LASER & PHOTONICS REVIEWS

www.lpr-journal.org

On-Chip Metamaterial Antenna Array with Distributed Bragg Deflector for Generation of Collimated Steerable Beams

Pablo Ginel-Moreno, Abdelfettah Hadij-ElHouati, Alejandro Sánchez-Postigo, J. Gonzalo Wangüemert-Pérez, Íñigo Molina-Fernández, Jens H. Schmid, Pavel Cheben, and Alejandro Ortega-Moñux*

The generation of collimated steerable beams of light is a fundamental function in optics needed in many applications, including free-space optical communications, remote sensing, and light detection and ranging. Implementing large-aperture light emitters directly on a photonic integrated chip without using external optics and expensive alignment systems is an outstanding challenge in integrated photonics. Here, the experimental demonstration of a new integrated antenna array architecture that uses a compact feeding circuit is reported. The design is based on an apodized Bragg deflector working as a low-loss (<0.3 dB) ultra-compact beam expander, which generates a 40-µm-wide on-chip Gaussian beam that illuminates a one-dimensional array of 112 optical antennas with a length of 1.5 mm. Each antenna comprises a metamaterial subwavelength grating waveguide core that is laterally loaded with an array of periodic radiative silicon segments. The device is fabricated on a 220-nm silicon-on-insulator platform using a single etch process with a minimum feature size of 80 nm. An antenna array with a power gain of 50 dB, a radiation efficiency of −3.8 dB, and a far-field angular divergence of 1.8° × 0.2°, in a wavelength range of 1500–1580 nm is presented.

1. Introduction

Integrated photonics holds the promise of practical solutions in many current research areas, including quantum photonics,[1,2] biology,[3,4] metrology,[5,6] telecommunications,[7,8] remote sensing,[9,10] and light detection and ranging (LIDAR).[11,12] In many of these applications, designing nanophotonic structures to generate off-chip radiation of highly collimated beams is challenging, especially when working in centimeter-scale or longer ranges, where optical beams with large Rayleigh lengths are required.

Silicon-on-insulator (SOI) is an established platform for the fabrication of photonic integrated circuits due to the compactness it offers. However, the development of large radiating apertures to achieve collimated beams remains an outstanding challenge, as it necessitates the use of weakly radiating perturbations, realizable only with specific fabrication processes which permit minimum feature sizes (MFS) below 10 nm.[13] Other platforms like silicon nitride (Si_3N_4) have been explored to accomplish on-chip mode expansion and radiation of collimated beams using conventional gratings,[10] but integration density is sacrificed for lower-index platforms. An interesting solution to achieve high performance antennas integrated on silicon chips without using special fabrication processes is the use of metamaterials and metasurfaces. A metamaterial is an artificially engineered material that exhibits specific electromagnetic properties.[14–16] This technique has been widely demonstrated for on-chip antenna design for millimeter-wave (mmWave) and terahertz (THz) integrated circuit applications.[17–21] Furthermore, metamaterial engineering has been recently adopted for the design of integrated optical antennas.[22]

Optical phased arrays (OPAs),[23–26] which combine the interference of multiple grating couplers, have been used to steer collimated beams in the desired direction off-chip. Nonetheless, each of the radiating elements that comprise the OPA needs to be modulated in amplitude and phase separately to achieve

P. Ginel-Moreno, A. Hadij-ElHouati, A. Sánchez-Postigo, J. G. Wangüemert-Pérez, Í. Molina-Fernández, A. Ortega-Moñux
Telecommunication Research Institute (TELMA)
Universidad de Málaga
Louis Pasteur 32, Málaga 29010, Spain
E-mail: pgm@ic.uma.es
J. H. Schmid, P. Cheben
National Research Council Canada
1200 Montreal Road, Bldg. M50, Ottawa K1A0R6, Canada

The ORCID identification number(s) for the author(s) of this article can be found under https://doi.org/10.1002/lpor.202200164

DOI: 10.1002/lpor.202200164

complete beam shaping and steering with the utmost possible control. This implies that, as the number of elements in the array increases, the feeding scheme and control electronics quickly grow in complexity, sometimes becoming prohibitive.[27] One of the most commonly used OPA architectures is the one-dimensional (1D)-OPA, comprising a 1D array of long travelling wave antennas. 1D-OPAs require only N phase shifters (where N is the number of antennas), which alleviates the complexity of the feeding circuits and electronics compared to 2D-OPAs, where the number of control elements typically grows as N^2. On the other hand, the steering mechanism of 1D-OPAs is typically based on phase differences between antennas and wavelength tuning, whereas in 2D-OPAs only phase differences are needed. In SOI platform, 1D-OPAs can achieve highly collimated beams with a beam divergence of ≈0.1° and a dynamic 2D-scanning with wavelength sensitivities of ≈0.14° nm^{-1}.[27–29] The feeding scheme of an OPA is an important part of the system architecture, directly affecting the scanning range and beamforming characteristics of the system. Two types of beam splitters for feeding schemes are typically being used, namely multimode interference (MMI) coupler trees and star couplers. The advantage of using MMI coupler trees is their simplicity. However, since all antennas usually receive the same amplitude, the array factor follows a periodic sinc function, which results in a limited sidelobe suppression ratio.[30–32] On the other hand, star couplers are particularly convenient for feeding many antennas within a compact small footprint, but they typically have a larger insertion loss.[26,33,34]

In this paper, we propose an ultracompact novel OPA feeding architecture which facilitates the adjustment of amplitude and phase of the different antennas as required for beam steering, while maintaining a simple structure of the system independent of the number of elements. The antenna array is composed of 112 millimeter-long surface-emitting antennas, as developed in our previous work,[22] leveraging subwavelength grating (SWG) metamaterial engineering. SWG engineered metamaterials, since their first demonstration in silicon photonics,[35,36] have been extensively used for overcoming performance limitations of conventional integrated photonic devices.[15,16,37,38] A distributed Bragg deflector (DBD)[39] with SWG metamaterial lateral cladding is first used to convert a strip waveguide mode into a wide beam on-chip with a very compact device structure. This wide beam with an amplitude and phase profile tailored by the DBD is then launched into the antenna array. The beam steering is achieved in both azimuthal and vertical directions directly by tuning the wavelength. The MFS of the device is 80 nm, which facilitates the fabrication in SOI by e-beam lithography or immersion deep-UV lithography.[40]

The device is demonstrated experimentally, radiating a collimated beam with a full-width at half-maximum (FWHM) angular divergence of 1.8° × 0.2°.

2. Description of the Device

The proposed device, shown schematically in **Figure 1**a, comprises two main parts: 1) an on-chip DBD to convert the fundamental mode of a conventional silicon strip waveguide into a slab-confined free-propagating collimated Gaussian beam and 2) a 1D-OPA of weak, millimeter-long free-space radiating antennas that are fed with the wide Gaussian beam.

The DBD, based on an architecture reported by the authors in ref. [39], is composed of an apodized sidewall grating waveguide that converts the TE-polarized mode of the input waveguide into a Gaussian beam confined in the silicon slab. The input light is coupled to the sidewall grating waveguide through an adiabatic transition. The waveguide mode is subsequently diffracted by the sidewall grating waveguide toward the lateral subwavelength grating metamaterial slab and coupled to a silicon slab. Due to its diffractive nature, the sidewall grating may also radiate light off-chip.[41] To suppress the off-chip radiation loss we leverage the single-beam condition by judiciously designing the DBD grating period Λ_{DBD}.[39] The loss penalty for coupling of the input waveguide mode to Gaussian beam propagating in the slab is <0.3 dB.

The resulting Gaussian beam has a mode field diameter (MFD) of 40 μm, which remains practically constant within the working band (1500–1580 nm). This MFD constitutes an unprecedented ~100 times beam width expansion achieved over a propagation distance as small as 80 μm. As shown in Figure 1a, the DBD forms an angle of 33° with respect to the y-axis, such that the diffracted beam propagates in the x-direction (perpendicular to the antenna array) at $\lambda_0 = 1540$ nm. The diffraction angle into the silicon slab changes with the operating wavelength $\phi_{slab}(\lambda)$, which provides a mechanism to steer the off-chip radiated beam, as will be discussed in Section 3.

Before reaching the OPA, the Gaussian beam travels through a 30-μm-long tapered adiabatic adaptation zone which connects the silicon slab to the antenna array (Figure 1b). The tapers minimize insertion losses and spurious reflections and discretize the beam profile generated by the Bragg deflector to feed each individual antenna with a specific amplitude and phase. The OPA is formed by 112 antennas arrayed in the transversal direction with a period $\Lambda_y = 1.45$ μm. A detailed description of the optical antennas can be found in our previous work.[22] The geometry of these antennas, shown in an inset of Figure 1, consists of an SWG core (width $W_{SWG} = 650$ nm and period $\Lambda_{SWG} = 170$ nm) that is loaded with an array of perturbation segments with a period $\Lambda_x = 4{\cdot}\Lambda_{SWG} = 680$ nm. The waveguide core of the antennas comprises a periodic structure operating in the subwavelength regime. In the latter, the SWG waveguide behaves as a metamaterial allowing accurately adjusment of electromagnetic parameters such as modal confinement and the effective index of the Floquet–Bloch mode supported in this waveguide. The SWG core is designed to reduce the mode confinement, thereby increasing the interaction with the lateral radiative segments. This architecture provides a precise control of the radiation strength by choosing the gap (g) between the SWG core and the lateral segments, while maintaining an MFS of 80 nm and minimally affecting the effective index of the Floquet–Bloch mode (n_{FB}).

The proposed OPA feeding circuit has several distinct advantages: First, by using a DBD to illuminate the antenna array, it is possible to generate a desired amplitude and phase profile of the wavefront that excites the individual antennas. Second, the device is very compact, capable of generating a wide Gaussian beam, with a minimum footprint of 80 μm × 160 μm, as shown in Figure 1a. Finally, beam steering in both azimuthal and vertical directions is achieved by using a DBD in conjunction with standard wavelength tuning of the array.

To efficiently design the DBD and the optical antenna used for the array, we performed Floquet–Bloch mode analysis of both

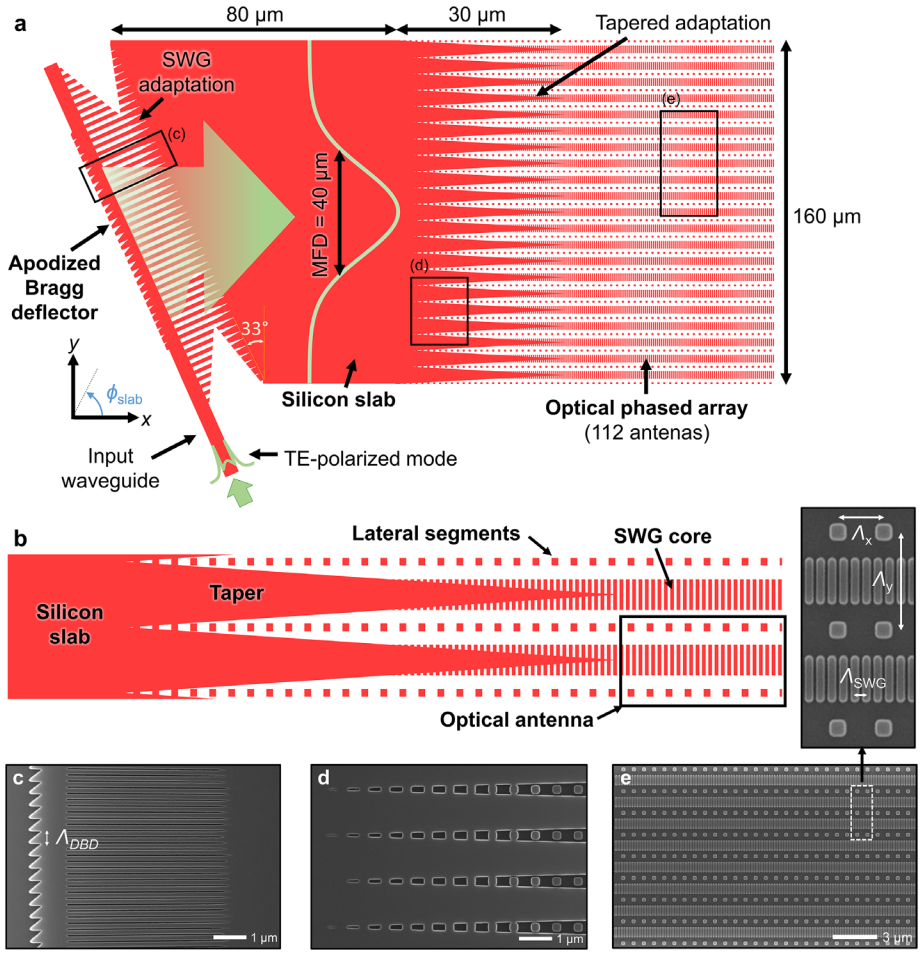

Figure 1. a) Top-view schematic of the device when a Si-wire waveguide mode enters the apodized Bragg deflector and is radiated into the silicon slab as a Gaussian beam with an MFD of 40 μm, to subsequently illuminate the OPA. b) Schematic of the transition between the silicon slab and two adjacent antennas. The taper samples the mode field in the slab and transfer it with a specific phase and amplitude into the SWG core, where the propagating field interacts with the lateral segments, i.e., radiative elements of the antenna. c) SEM image of a section of the apodized Bragg deflector and the SWG adaptation region. d) SEM image of the tapered adaptation region between the silicon slab and the OPA. e) SEM image of an OPA section, with the long antennas arrayed in transversal direction (y).

structures by using 3D full-vectorial FDTD (finite difference time domain) simulations of a single period Λ. The method consists of setting periodic boundary conditions at $x = 0$ and $x = \Lambda$, then enforcing a relative phase shift between the boundaries and exciting the structure with a broadband source. This allows us to characterize the Floquet–Bloch modes by determining the complex resonant frequencies.[42]

The device was fabricated on a 220-nm SOI platform with a 2-μm buried oxide (BOX) layer and was patterned using electron-beam lithography and reactive-ion-etching, with all structures fully etched. A 2.2-μm thick upper SiO_2 cladding was deposited by chemical vapor deposition. Finally, the chip facets were defined with a deep-etch process. Figure 1c–e shows scanning electron microscope (SEM) images of a section of the fabricated Bragg deflector including the SWG adaptation zone, the tapered adaptation section between the silicon slab and the antenna array, and a portion of the OPA, respectively.

In the following, we present a study of the complete device when the light source wavelength is tuned, and we analyze the performance of the OPA in terms of far-field radiation and beam shaping.

3. Fundamentals and Simulation

For antennas arrayed in transversal direction (y), the far-field radiation amplitude $F(\theta, \phi)$ is defined as the product of the far field of a single antenna $R(\theta, \phi)$ and the array factor $A(\theta, \phi)$, i.e., $F(\theta, \phi) = R(\theta, \phi) \times A(\theta, \phi)$.[29] The array factor depends on the amplitude and phase of each antenna and can be calculated as[43]

$$A\ (\theta,\ \phi) = \sum_n C_n e^{jkd_n \sin\theta \sin\phi} \tag{1}$$

where C_n is the complex amplitude of the nth antenna, k is the wavenumber in the medium where the far field is being calculated, and d_n is the distance from the origin of each antenna in transversal direction (y). A specific input excitation of the antenna array will determine the value of the complex amplitudes C_n and

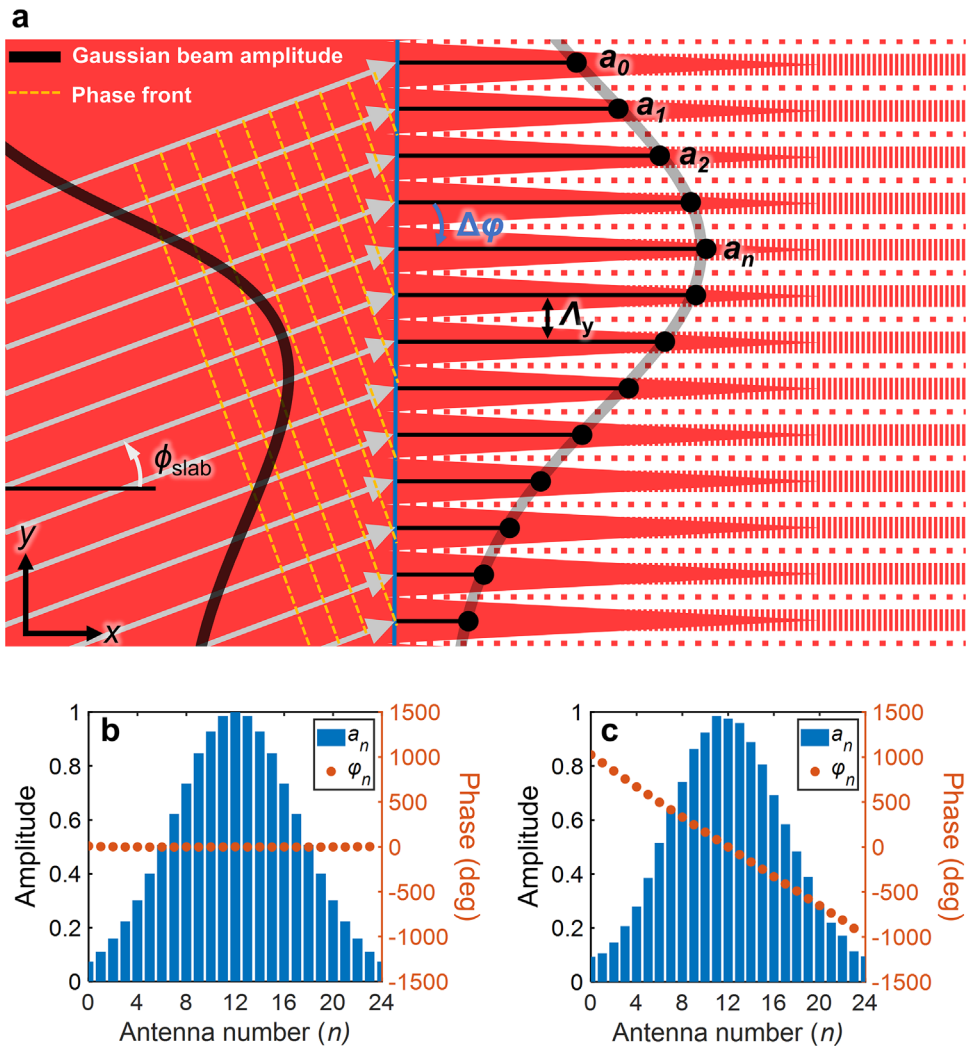

Figure 2. a) Schematic of the OPA feeding geometry when a Gaussian beam is incident at an angle ϕ_{slab}. Each taper discretizes the illumination from the silicon slab, yielding an amplitude a_n and a phase φ_n, with a linear relative phase $\Delta\varphi$ between adjacent antennas. 2D FDTD simulation of a Gaussian beam with 20 μm diameter incident to an OPA of 25 antennas with b) $\phi_{slab} = 0°$ and c) $\phi_{slab} = -5°$.

thus the array factor $A(\theta, \phi)$. Accordingly, the illumination generated by the DBD will determine the size and shape of the radiated beam as well as the azimuthal direction in which the radiation intensity will be maximal in the air (θ_0, ϕ_0).

Figure 2a shows a schematic view of the beam diffracted by the DBD to the silicon slab illuminating the OPA with a Gaussian intensity profile at an angle ϕ_{slab} with the x-axis. Both the amplitude and phase of the Gaussian wavefront are sampled by each taper connected to the slab, and in turn each taper will input an amplitude (a_n) and phase (φ_n) to the nth SWG waveguide with radiating segments forming the nth antenna. The angled wavefront sets the individual phase of each antenna (φ_n), having a linear relative phase difference between the adjacent antennas

$$\Delta\varphi = \varphi_{n+1} - \varphi_n = \frac{2\pi}{\lambda} n_{slab} \Lambda_y \sin\phi_{slab} \tag{2}$$

where n_{slab} is the effective index of the TE-polarized mode of the silicon slab, Λ_y is the transversal period of the array elements, and ϕ_{slab} is the incident angle of the on-chip beam to the OPA. The tapered adaptation zone reduces possible reflections between the slab and the OPA, and sample the field of the slab, feeding each antenna with a complex amplitude

$$C_n = a_n \, e^{j\varphi_n} = a_n \, e^{jn\Delta\varphi} \tag{3}$$

where a_n is the amplitude of the incident beam, φ_n is the phase of the wavefront at the input of each taper, and $\Delta\varphi$ is the relative phase among adjacent antennas, as previously defined. 2D FDTD simulations have been carried out to investigate taper sampling of amplitude and phase when an on-chip Gaussian beam incides at OPA at different angles. We use a Gaussian beam of 20 μm diameter and a small OPA comprising 25 antennas, for $\phi_{slab} = 0°$ (Figure 2b) and $\phi_{slab} = -5°$ (Figure 2c). It is observed that the Gaussian envelope is identical for both illumination angles, while a relative phase difference between antennas is introduced for off-axis illumination $(\phi_{slab} = -5°)$.

The OPA comprises 112 metamaterial-engineered surface-emitting antennas, arrayed along the y-direction with a period Λ_y, as schematically shown in **Figure 3**a. To represent the OPA far field, we use a convenient coordinate system[26] where θ is the vertical angle and ϕ is the azimuthal angle projected into the plane of the camera used to measure the far field. The antenna radiation angle is controlled by tuning the wavelength, according to the grating equation[44]

$$\sin\theta_0 = n_c \sin\theta_c = n_{FB} - \frac{\lambda}{\Lambda_x} \tag{4}$$

where θ_0 and θ_c are the emission angles in the air and the upper cladding, respectively, n_c is the refractive index of the upper silica cladding, n_{FB} is the Floquet–Bloch mode effective index, Λ_x is the period of the array of radiative segments, and λ is the wavelength.

The elemental antenna has been designed by Floquet–Bloch analysis for a TE-polarized SWG waveguide mode radiating into the air at $\theta_0 = -25°$ at the central wavelength $\lambda_0 = 1540$ nm. The far-field diagram of a mm-long elemental antenna $R(\theta, \phi)$ corresponds to a highly collimated beam in the vertical direction (θ). Figure 3b shows the calculated emission angle θ_0 of the elemental antenna as a function of the wavelength for the nominal structure and two designs with ±20 nm lithography bias, with a wavelength tuning sensitivity of $\partial\theta/\partial\lambda \sim -0.14°\ \mathrm{nm}^{-1}$.

The DBD is employed to control the on-chip angle ϕ_{slab} (see Figure 2) of the diffracted Gaussian beam by tuning the wavelength, leveraging the intrinsic dispersion of the deflector. Figure 3c shows the steering angle in the silicon slab waveguide, ϕ_{slab} as a function of wavelength. A variation in the on-chip angle (ϕ_{slab}) will cause a deviation in the air of the main beam in the azimuthal direction (ϕ_0). The calculated wavelength tuning sensitivity in the slab waveguide is $\partial\phi_{slab}/\partial\lambda = -0.086°\ \mathrm{nm}^{-1}$, corresponding to $\partial\phi/\partial\lambda = 0.26°\ \mathrm{nm}^{-1}$ when the beam is out-coupled from the chip to the air.

A distinct advantage of our device is its intrinsic apodization property. Diffraction by the DBD results in a Gaussian field profile in the slab waveguide, which is subsequently used to illuminate the antenna array. This Gaussian apodization effectively suppresses the side-lobes near the main peak of the collimated beam in the transversal direction of the far field, as shown in Figure 3d–f. This is an important advantage compared to conventional OPAs where the light is distributed on-chip through a tree of power splitters yielding uniform intensity across different antennas in the array. This uniform intensity profile results in the array factor modified with a sinc function and corresponding side-lobes near the main peak of the far field (on the order of −13 dB[43]). This effect is efficiently suppressed in our highly compact apodized device, which presents no sidelobes in azimuthal direction (ϕ). Near the central wavelength ($\lambda_0 = 1540$ nm), the antenna array has $\mathrm{FWHM}_\theta \sim 0.06°$ and $\mathrm{FWHM}_\phi \sim 1.74°$, in vertical and azimuthal directions, respectively. While the former is determined by the antenna length of 1.5 mm, the latter corresponds to an illumination of the OPA with a Gaussian beam of ≈40 μm diameter.

Using the parameters typically employed in radiofrequency antenna design, our antenna array has a directivity of 53 dBi (decibels related to isotropic) near the central wavelength of the design. This constitutes an enhancement of 13 dB compared to a single antenna, according to the definition of directivity[43]

$$D = \frac{4\pi}{\iint g(\theta,\phi)\,\mathrm{d}\Omega} = \frac{4\pi}{\Omega_s} \tag{5}$$

where $g(\theta, \phi)$ is the normalized radiation intensity and Ω_s is the beam solid angle. The directivity of both the single antenna and array are shown in **Figure 4**a. Another important parameter to characterize the antenna array is the power gain, which is defined by multiplying the directivity by the power efficiency of the feeding stage. The latter is affected by both the losses in the SWG adaptation between the DBD and the silicon slab (η_{slab}) and the losses in the tapered multi-waveguide region that connects the silicon slab to the OPA (η_{taper}). We performed 3D FDTD simulations to estimate the power efficiency in these two regions and the results are shown in Figure 4b. The total power efficiency of the feeding stage at the central wavelength is around −0.5 dB, which is much better than typical feeding stages used in OPAs. The power gain of the antenna can be estimated by the product of the power efficiency and the directivity, obtaining the result shown in Figure 4c. Finally, in our antenna, the vertical symmetry is broken by a silicon substrate underneath the BOX, and some of the power radiated downward is reflected at the BOX–substrate interface and interferes (constructively or destructively) with the power radiated upward. In integrated optics, grating directionality is often defined as the ratio of upward radiated power to the total radiated power. In our design, the grating directionality is about −3 dB. Considering the latter and the total system losses calculated above, the radiation efficiency or the amount of total power radiated off-chip in the desired direction (P_{up}) compared to the total power delivered to the system (P_T) is shown in Figure 4d.

4. Experimental Results

To experimentally characterize our device, we used the Agilent 81600B tunable laser with an external polarization controller to select in-plane (TE) polarization at the chip input. The light is coupled to the chip from a lensed fiber via a metamaterial fiber-chip coupler[45] followed by a nominal 500-nm-wide interconnecting waveguide.

The measured far-field intensity pattern radiated by the antenna array as the wavelength is scanned is shown in **Figure 5**a. This measurement was made using an infrared camera with an InGaAs sensor array of 320 × 256 pixels and a pitch of 30 μm. The system includes an anti-reflection coated achromatic lens with a focal length f = 35 mm. The InGasAs sensor array is positioned at the focal plane of the lens, and the system forms the far-field distribution as the 2D Fourier transform of the near field of the antenna array. While the optical setup used together with the sensor size limits the scanning range to 15.8° × 12.6°, this is sufficient to demonstrate the proof-of-concept device operation. This is clearly observed in Figure 5a, showing the measured radiated far field of the antenna array scanning diagonally with wavelength. As the wavelength tuning varies the diffraction angle of the DBD, it modifies the relative phases between the antennas, hence scanning the radiated beam in ϕ direction while at the same time the wavelength tuning changes the emission angle of the antennas in

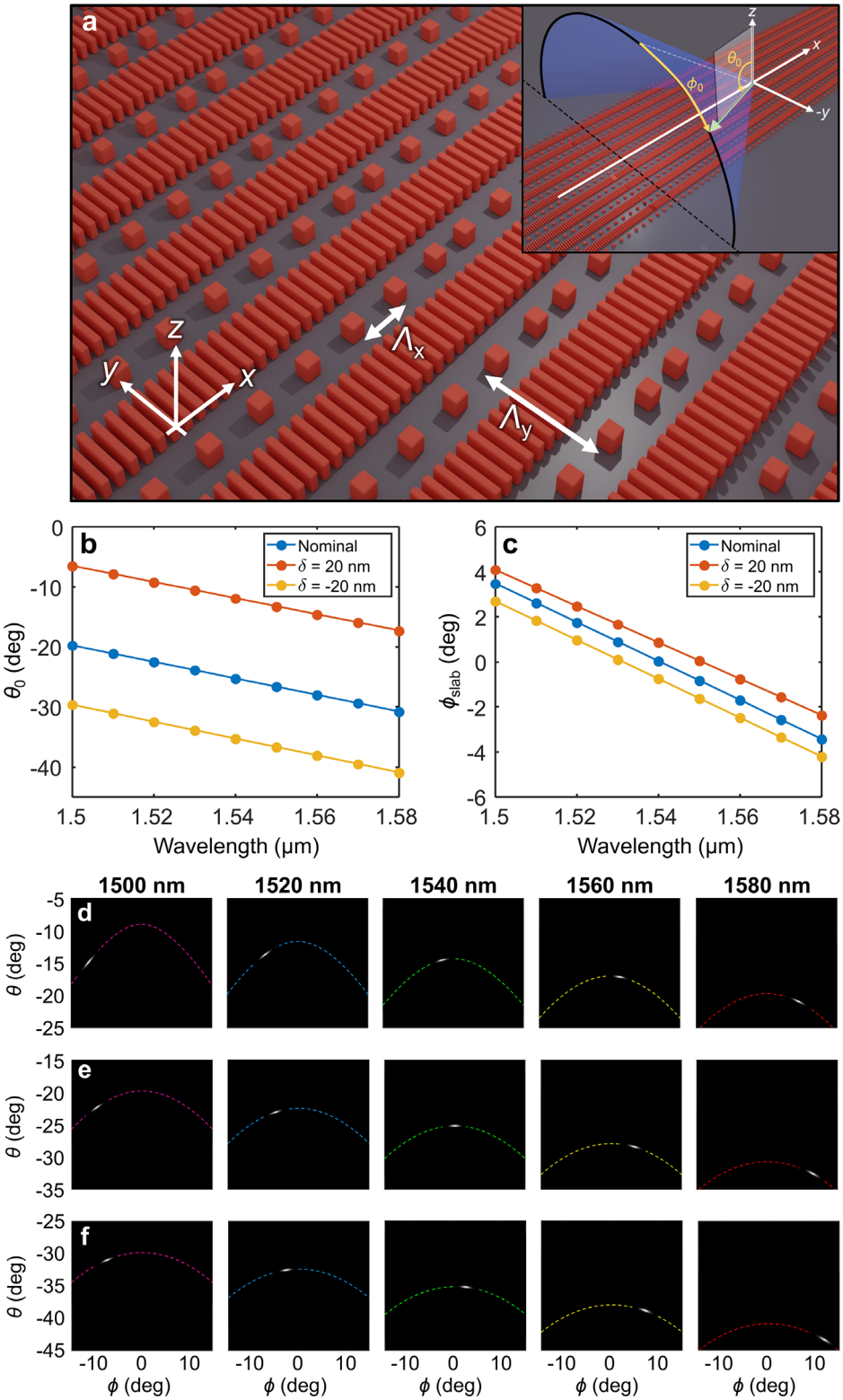

Figure 3. a) A schematic view of the array of surface-emitting silicon antennas. The inset shows the light cone radiated by a grating, which denotes the angular range available for the radiated beam.[26] b) Vertical θ_0 and c) lateral ϕ_{slab} steering as a function of wavelength for the nominal design and ±20 nm fabrication bias. d–f) Calculated far-field intensity distributions of the spot radiated by the OPA when it is fed with the DBD for +20 nm lithography bias, nominal design, and −20 nm lithography bias, respectively. The elliptical contours are the projections of the cone in the plane of the camera, for different wavelengths (columns) and bias errors (rows). Notice also that the maximum of the projected ellipse corresponds to the single antenna case shown in (b).

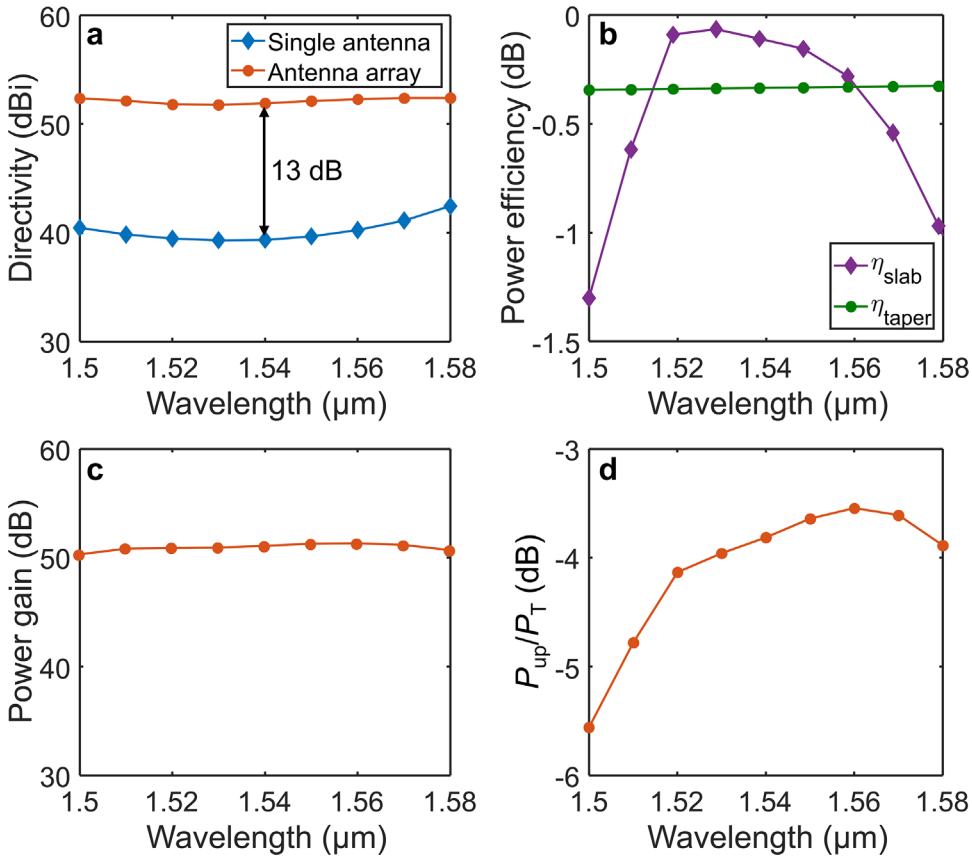

Figure 4. a) Comparison between the directivity of a single antenna and the antenna array. b) Power efficiency in different sections, i.e., the transition between the DBD and the silicon slab and the transition between slab and antenna array. c) Power gain of the antenna array. d) Fraction of total power radiated off-chip into the desired direction compared with the total power delivered to the system, including the effect of directionality.

the θ direction. The superposition of these two effects results in diagonal beam steering. A comparison between simulation and experimental results is presented in Figure 5b,c, where the emission angles ϕ and θ are shown as a function of the wavelength. The wavelength scanning sensitivity determined from the slope of the curves for both azimuthal ($\partial\phi/\partial\lambda$) and vertical ($\partial\theta/\partial\lambda$) directions is close to the theoretical prediction. The observed shift in the experimental curves can be explained by including in the simulations the effect of under-etching, i.e., bias in the fabrication process of ≈20 nm, which was confirmed by SEM inspection.

We also characterized the angular divergence of the radiated beam. In **Figure 6**a, we show the far-field intensity cross-sections for both directions (θ and ϕ) of the beam spot measured at λ = 1575 nm, which is radiating approximately at $\phi = 0°$. The far-field distribution is related to the near field via the Fourier transform. Thus, the far-field vertical profile is expected to follow a Lorentzian function since the near-field radiation pattern is exponential, as the radiative segments are arrayed uniformly with constant radiation strength along the longitudinal direction (x), i.e., without apodization in this direction. On the other hand, the far-field azimuthal profile is determined by the antenna array excitation along the transversal direction (y). The latter is intrinsically apodized by a Gaussian profile in the slab waveguide as generated by the DBD illumination, which in turn results in a Gaussian far-field in the azimuthal direction. This is also confirmed by the experimental results illustrated in Figure 6a, showing a Gaussian far-field in azimuthal direction and a narrow Lorentzian-like profile in the vertical direction.

The angular divergence of the radiated beam in azimuthal direction can be calculated as[46]

$$\mathrm{FWHM}_{\phi} = \frac{\lambda}{\pi w_0}\sqrt{2\ln 2} \tag{6}$$

where w_0 is the radius of the Gaussian beam illuminating the antenna array. The measured FWHM is shown in Figure 6b for both directions. In the azimuthal direction, the experimental results yield a good agreement with Equation (6). In the vertical direction, the measured FWHM_{θ} is wider than expected from the simulations, which indicates that the effective length of the antenna is shorter than designed. This is also consistent with the observation that the angular divergence is nearly constant with wavelength, as shown in Figure 6b. The higher grating strength shortens the effective antenna lengths.

5. Conclusion

We designed and experimentally demonstrated a radically new topology to implement 1D antenna arrays. A DBD is used as a feeder element to form a Gaussian beam propagating in a

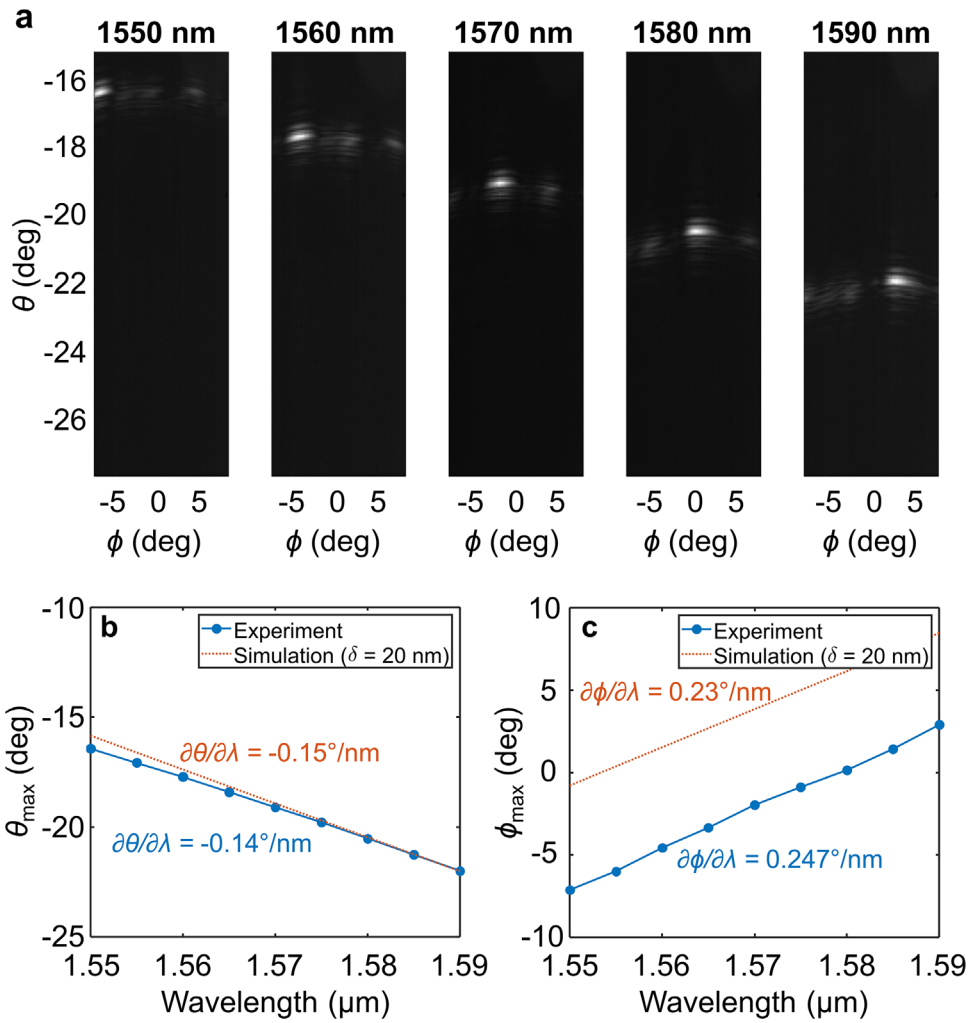

Figure 5. a) Measured far-field intensity distribution as a function of θ and ϕ angular coordinates for different wavelengths in the range of 1550–1590 nm. b) Measured vertical emission angle and c) azimuthal emission angle as a function of the wavelength. For both cases, the wavelength sensitivity is estimated as the slope of a linear fit. The curves are compared with the simulation results for the device with the fabrication bias of 20 nm.

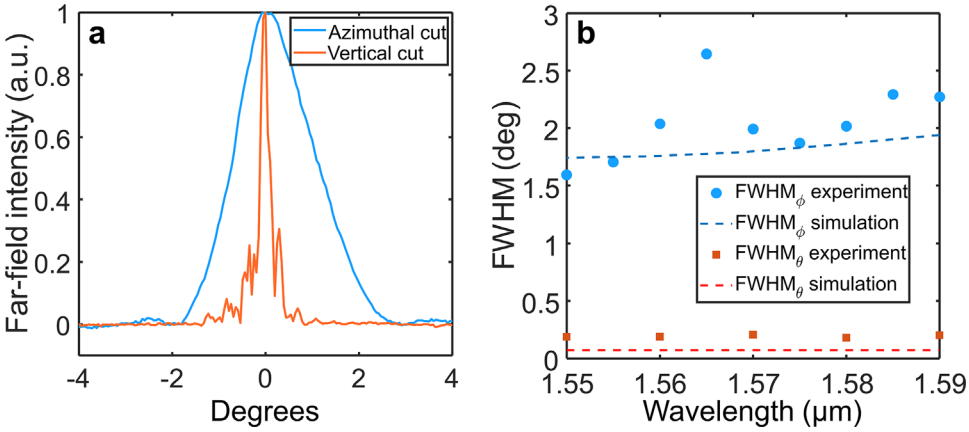

Figure 6. a) Far-field intensity along the azimuthal and vertical directions. b) Measured angular divergence in azimuthal direction and in vertical direction as a function of the wavelength, and the corresponding 3D FDTD simulation results.

slab waveguide with a wavelength-controllable phase tilt, subsequently coupled to an array of long metamaterial-engineered nanophotonic antennas. This allows beam steering in both azimuthal and vertical directions by using a single control parameter, i.e., scanning the wavelength. Another advantage of our device is the compact size of the feeder, in this example only 80 μm × 160 μm, which is significantly smaller than the state-of-the-art power-splitting trees commonly used for feeding 1D-OPAs. At the same time, the DBD feeder acts as a self-apodizing element, yielding a Gaussian far-field profile, without typical sidelobes associated with the sinc function in OPAs with nonapodized apertures. The device was experimentally demonstrated obtaining a highly collimated beam in the far field with an FWHM angular divergence of 1.8° × 0.2°. The ability to illuminate a complete OPA with a DBD and achieve beam steering in both azimuthal and vertical direction by using a single control parameter as demonstrated in this work is an important advance toward the development of complex 2D beam steering systems with a minimum number of actuating elements. We envision that building upon the concept demonstrated in this work, full 2D beam steering can be ultimately achieved by introducing an additional scanning parameter, e.g., thermo-optic actuation. We believe that our results establish exceptional prospects for the implementation of 1D-OPAs for free-space optical interconnects and remote sensing applications leveraging established integrated silicon photonic technology.

Acknowledgements

This work was supported by the High Throughput and Secure Networks Challenge Program at the National Research Council of Canada (HTSN 209); Ministerio de Ciencia, Innovación y Universidades (MCIU) (PID2019-106747RB-I00); Ministerio de Universidades (FPU16/03401, FPU20/03487); Junta de Andalucía (P18-RT-1453, P18-RT-793); FEDER Andalucía (UMA20-FEDERJA-158); Universidad de Málaga. Funding for open access charge from Universidad de Málaga/CBUA is acknowledged.

Conflict of Interest

The authors declare no conflict of interest.

Data Availability Statement

The data that support the findings of this study are available from the corresponding author upon reasonable request.

Keywords

Bragg structures, Fourier optics, optical antennas, optical phased arrays, silicon photonics, subwavelength grating metamaterials

Received: April 24, 2022
Published online:

[1] A. W. Elshaari, W. Pernice, K. Srinivasan, O. Benson, V. Zwiller, *Nat. Photonics* **2020**, *14*, 285.
[2] J. Wang, F. Sciarrino, A. Laing, M. G. Thompson, *Nat. Photonics* **2020**, *14*, 273.
[3] J. Juan Colás, in *Dual-Mode Electro-Photonic Silicon Biosensors*, Springer, New York **2017**, pp. 59–93.
[4] R. Soref, *Nat. Photonics* **2010**, *4*, 495.
[5] A. Bag, M. Neugebauer, U. Mick, S. Christiansen, S. A. Schulz, P. Banzer, *Nat. Commun.* **2020**, *11*, 2915.
[6] D. T. Spencer, T. Drake, T. C. Briles, J. Stone, L. C. Sinclair, C. Fredrick, Q. Li, D. Westly, B. R. Ilic, A. Bluestone, N. Volet, T. Komljenovic, L. Chang, S. H. Lee, D. Y. Oh, M.-G. Suh, K. Y. Yang, M. H. P. Pfeiffer, T. J. Kippenberg, E. Norberg, L. Theogarajan, K. Vahala, N. R. Newbury, K. Srinivasan, J. E. Bowers, S. A. Diddams, S. B. Papp, *Nature* **2018**, *557*, 81.
[7] A. H. Atabaki, S. Moazeni, F. Pavanello, H. Gevorgyan, J. Notaros, L. Alloatti, M. T. Wade, C. Sun, S. A. Kruger, H. Meng, K. Al Qubaisi, I. Wang, B. Zhang, A. Khilo, C. V. Baiocco, M. A. Popović, V. M. Stojanović, R. J. Ram, *Nature* **2018**, *556*, 349.
[8] C. Sun, M. T. Wade, Y. Lee, J. S. Orcutt, L. Alloatti, M. S. Georgas, A. S. Waterman, J. M. Shainline, R. R. Avizienis, S. Lin, B. R. Moss, R. Kumar, F. Pavanello, A. H. Atabaki, H. M. Cook, A. J. Ou, J. C. Leu, Y.-H. Chen, K. Asanović, R. J. Ram, M. A. Popović, V. M. Stojanović, *Nature* **2015**, *528*, 534.
[9] R. Baets, in *Optical Fiber Communication Conference (OFC) 2021*, (Eds: P. Dong, J. Kani, C. Xie, R. Casellas, C. Cole, M. Li), Optica Publishing Group, Washington D.C. **2021**, p. W1D.1.
[10] S. Kim, D. A. Westly, B. J. Roxworthy, Q. Li, A. Yulaev, K. Srinivasan, V. A. Aksyuk, *Light: Sci. Appl.* **2018**, *7*, 72.
[11] C. V. Poulton, M. J. Byrd, P. Russo, E. Timurdogan, M. Khandaker, D. Vermeulen, M. R. Watts, *IEEE J. Sel. Top. Quantum Electron.* **2019**, *25*, 7700108.
[12] J. Sun, E. Timurdogan, A. Yaacobi, E. S. Hosseini, M. R. Watts, *Nature* **2013**, *493*, 195.
[13] S. A. Miller, Y.-C. Chang, C. T. Phare, M. C. Shin, M. Zadka, S. P. Roberts, B. Stern, X. Ji, A. Mohanty, O. A. Jimenez Gordillo, U. D. Dave, M. Lipson, *Optica* **2020**, *7*, 3.
[14] I. Staude, J. Schilling, *Nat. Photonics* **2017**, *11*, 274.
[15] P. Cheben, R. Halir, J. H. Schmid, H. A. Atwater, D. R. Smith, *Nature* **2018**, *560*, 565.
[16] J. M. Luque-González, A. Sánchez-Postigo, A. Hadij-ElHouati, A. Ortega-Moñux, J. G. Wangüemert-Pérez, J. H. Schmid, P. Cheben, Í. Molina-Fernández, R. Halir, *Nanophotonics* **2021**, *10*, 2765.
[17] Y. Dong, T. Itoh, *Proc. IEEE* **2012**, *100*, 2271.
[18] M. Alibakhshikenari, B. S. Virdee, C. H. See, P. Shukla, S. Salekzamankhani, R. A. Abd-Alhameed, F. Falcone, E. Limiti, *Sci. Rep.* **2020**, *10*, 11034.
[19] M. Alibakhshikenari, B. S. Virdee, S. Salekzamankhani, S. Aïssa, C. H. See, N. Soin, S. J. Fishlock, A. A. Althuwayb, R. Abd-Alhameed, I. Huynen, J. A. McLaughlin, F. Falcone, E. Limiti, *Sci. Rep.* **2021**, *11*, 10218.
[20] M. Alibakhshikenari, E. M. Ali, M. Soruri, M. Dalarsson, M. Naser-Moghadasi, B. S. Virdee, C. Stefanovic, A. Pietrenko-Dabrowska, S. Koziel, S. Szczepanski, E. Limiti, *IEEE Access* **2022**, *10*, 3668.
[21] M. Alibakhshikenari, B. S. Virdee, A. A. Althuwayb, S. Aïssa, C. H. See, R. A. Abd-Alhameed, F. Falcone, E. Limiti, *J. Infrared, Millimeter, Terahertz Waves* **2021**, *42*, 17.
[22] P. Ginel-Moreno, A. Sánchez-Postigo, J. de-Oliva-Rubio, A. Hadij-ElHouati, W. N. Ye, J. G. Wangüemert-Pérez, Í. Molina-Fernández, J. H. Schmid, P. Cheben, A. Ortega-Moñux, *Opt. Lett.* **2021**, *46*, 3733.
[23] Q. Wang, S. Wang, L. Jia, Y. Cai, W. Yue, M. Yu, *Opt. Express* **2021**, *29*, 10509.
[24] R. Fatemi, A. Khachaturian, A. Hajimiri, *IEEE J. Solid-State Circuits* **2019**, *54*, 1200.
[25] P. Wang, G. Luo, Y. Xu, Y. Li, Y. Su, J. Ma, R. Wang, Z. Yang, X. Zhou, Y. Zhang, J. Pan, *Photonics Res.* **2020**, *8*, 912.

[26] D. N. Hutchison, J. Sun, J. K. Doylend, R. Kumar, J. Heck, W. Kim, C. T. Phare, A. Feshali, H. Rong, *Optica* **2016**, *3*, 887.
[27] M. J. R. Heck, *Nanophotonics* **2017**, *6*, 93.
[28] J. He, T. Dong, Y. Xu, *IEEE Access* **2020**, *8*, 188284.
[29] Y. Guo, Y. Guo, C. Li, H. Zhang, X. Zhou, L. Zhang, *Appl. Sci.* **2021**, *11*, 4017.
[30] D. Kwong, A. Hosseini, J. Covey, Y. Zhang, X. Xu, H. Subbaraman, R. T. Chen, *Opt. Lett.* **2014**, *39*, 941.
[31] C. V. Poulton, M. J. Byrd, M. Raval, Z. Su, N. Li, E. Timurdogan, D. Coolbaugh, D. Vermeulen, M. R. Watts, *Opt. Lett.* **2017**, *42*, 21.
[32] G. Kang, S.-H. Kim, J.-B. You, D.-S. Lee, H. Yoon, Y.-G. Ha, J.-H. Kim, D.-E. Yoo, D.-W. Lee, C.-H. Youn, K. Yu, H.-H. Park, *IEEE Photonics Technol. Lett.* **2019**, *31*, 1685.
[33] K. Van Acoleyen, K. Komorowska, W. Bogaerts, R. Baets, *J. Lightwave Technol.* **2011**, *29*, 3500.
[34] P. Munoz, P. Daniel, L. A. Bru, G. Mico Cabanes, J. Benitez, D. Goodwill, E. Bernier, *IEEE J. Sel. Top. Quantum Electron.* **2022**, *28*, 1.
[35] P. Cheben, D.-X. Xu, S. Janz, A. Densmore, *Opt. Express* **2006**, *14*, 4695.
[36] P. Cheben, P. J. Bock, J. H. Schmid, J. Lapointe, S. Janz, D.-X. Xu, A. Densmore, A. Delâge, B. Lamontagne, T. J. Hall, *Opt. Lett.* **2010**, *35*, 2526.
[37] R. Halir, A. Ortega-Moñux, D. Benedikovic, G. Z. Mashanovich, J. G. Wangüemert-Pérez, J. H. Schmid, Í. Molina-Fernández, P. Cheben, *Proc. IEEE* **2018**, *106*, 2144.
[38] R. Halir, P. J. Bock, P. Cheben, A. Ortega-Moñux, C. Alonso-Ramos, J. H. Schmid, J. Lapointe, D.-X. Xu, J. G. Wangüemert-Pérez, Í. Molina-Fernández, S. Janz, *Laser Photonics Rev.* **2015**, *9*, 25.
[39] A. Hadij-ElHouati, P. Cheben, A. Ortega-Moñux, J. G. Wangüemert-Pérez, R. Halir, J. de-Oliva-Rubio, J. H. Schmid, I. Molina-Fernández, *Opt. Lett.* **2021**, *46*, 2409.
[40] E. Luan, V. Donzella, K. Cheung, L. Chrostowski, in *2019 24th OptoElectronics and Communications Conf. (OECC) and 2019 Int. Conf. Photonics in Switching and Computing (PSC)*, IEEE, Piscataway, NJ, **2019**, pp. 1–3.
[41] A. Hadij-ElHouati, P. Cheben, A. Ortega-Moñux, J. G. Wangüemert-Pérez, R. Halir, J. H. Schmid, Í. Molina-Fernández, *Opt. Express* **2019**, *27*, 33180.
[42] A. Taflove, S. C. Hagness, M. Piket-May, in *Computational Electromagnetics: The Finite-Difference Time-Domain Method*, (Eds: G. Burr, S. C. Hagness, A. Taflove), Elsevier Amsterdam, The Netherlands **2005**, Ch. 16.
[43] S. J. Orfanidis, *Electromagnetic Waves and Antennas*, **2003**.
[44] T. Tamir, S. T. Peng, *Appl. Phys.* **1977**, *14*, 235.
[45] P. Cheben, J. H. Schmid, S. Wang, D.-X. Xu, M. Vachon, S. Janz, J. Lapointe, Y. Painchaud, M.-J. Picard, *Opt. Express* **2015**, *23*, 22553.
[46] B. E. Saleh, M. C. Teich, *Fundamentals of Photonics*, John Wiley & Sons, New York **2019**.